Invigoration of convection by an overrunning diabatically modified cloud-top layer

Accepted at QJRMS 20 October 2017

K.A. Browning[a], D.J. Smart[b]

[a] *Independent researcher, Ambleside, UK;* [b] *Department of Earth Sciences, UCL Hazard Centre, UCL, London, UK.*

*Correspondence to: DJ Smart, UCL Hazard Centre, Kathleen Lonsdale Building, University College London, Gower St., London, WC1E 6BT. E-mail: d.smart@ucl.ac.uk

This paper investigates the factors that invigorated an outbreak of warm-sector convection which was instrumental in transporting high momentum downwards to give damaging surface winds. We have re-examined a wintertime extratropical cyclone from the Fronts and Atlantic Storm-Track EXperiment for which an earlier study had shown the warm-sector convection to be in the form of a series of arc-shaped rainbands. Using a 5-km grid version of the WRF (Weather Research and Forecasting) model, we show that this convection was enhanced as a result of the properties of an airstream at the base of the Dry Intrusion that overran the shallow moist zone (SMZ) of the warm sector. This airstream, which we refer to as the Diabatically Modified Cloud-Top Layer (DMCTL), is shown to have originated several hours earlier in part of an ana-cold frontal cloud layer where a region of previously ascending air began systematically to descend. Air from the DMCTL descended from heights of 2–3 km to heights of 1–2 km over a roughly 5-hour period during which sustained evaporation occurred and its potential temperature dropped by up to 5 C. This substantially enhanced the convective instability where this airstream overran the SMZ, leading to vigorous boundary-layer convection. The same region of evaporative cooling is also shown to have generated positive potential vorticity in the upper parts of the DMCTL, with values reaching about 3 PV units where it overran the SMZ. This layer of high PV, although we have not quantified its impact, may have increased the convective instability further by inducing differential advection below it. The cyclone in the present study later underwent frontal fracture and developed a cloud head but the processes diagnosed in this study were underway before the transition occurred. **Copyright © 2017 Royal Meteorological Society**

Key Words: extratropical cyclone; FASTEX; sting jet; damaging winds; WRF model; evaporative cooling

Received . . .

Citation: . . .

1. Introduction

This paper presents a case study motivated by the need to understand the cause of damaging surface wind gusts that occurred at an early stage in the development of an extratropical cyclone. The damaging winds were associated with shallow but vigorous boundary-layer convection within the dry slot of the incipient cyclone. A dry slot is a region, generally identified in satellite imagery, close to and equatorwards of the cyclone centre: it is characterised by extensive clearance of middle- and upper-level cloud as a result of an overrunning stream of dry air known as a

dry intrusion, hereafter 'DI' (Young *et al.* 1987; Browning 1997). A DI has a low wet-bulb potential temperature (θ_w) and, where it overruns a warm sector characterised by a shallow moist zone (SMZ) with a higher θ_w, it leads to potential instability as described in the split-front model of Browning and Monk (1982). Therefore, although the weather is indeed often dry in the dry slot, there is nevertheless the potential for outbreaks of convection. It has been known for some time (*e.g.* Carr and Millard 1985) that lines of convection do sometimes occur within dry slots. Such convection can lead to strong surface wind gusts by helping high momentum from the airstream just above the boundary layer to be transported down to the surface. One such occasion in the United Kingdom was described by Browning and Roberts (1999; hereafter BR99) who presented an analysis of a set of arc-shaped convective rainbands that gave rise to damaging winds in the dry slot of an incipient cyclone observed in Intensive Observational Period IOP 18A of the Fronts and Atlantic Storm-Track Experiment (FASTEX; Joly *et al.* 1999).

The study in the present paper revisits the case investigated in BR99. The original study showed that the convective rainbands within the dry slot produced surface gusts of up to 35 $\mathrm{m\,s^{-1}}$, causing severe damage in places. Two minor, but damaging, tornadoes were also reported as the system crossed southern England (TORRO (Tornado and Storm Research Organisation) database, accessed 31/01/2017). The rainbands were associated with an area of winds in excess of 40 $\mathrm{m\,s^{-1}}$ just above the SMZ. The original study combined a mesoscale analysis of observational data with the output from the mesoscale version of the operational Met Office Unified Model (15-km grid and 31 levels); however, despite the model benefiting from the assimilation of 3-hourly sequences of special rawinsonde ascents from several sites as part of FASTEX, the model was unable to reproduce the characteristic arc-shaped rainbands of that event.

In the time since that study was undertaken there have been improvements in the design of mesoscale models and in the quality of the datasets available for initializing them. In the present study we have succeeded in reproducing a set of arc rainbands in the dry slot observed in FASTEX IOP 18A by using a version of the WRF (Weather Research and Forecasting) model (Skamarock *et al.*, 2008) run with a 5 km grid and 48 levels (model top at 50 hPa). The model was initialized with data from the European Centre for Medium-Range Weather Forecasts (ECMWF) ERA-Interim reanalysis (Dee *et al.* 2011). Because of our increased confidence in the realism of the model results we have used the model to carry out an in-depth analysis of the mesoscale factors that contributed to the vigour of the convection on this occasion.

The cyclone in this study underwent frontal fracture as described by Shapiro and Keyser (1990). Cyclones conforming to the Shapiro-Keyser model go through four stages of evolution characterised by: (i) an incipient frontal cyclone, (ii) frontal fracture, (iii) bent-back warm front and, (iv) warm-core frontal seclusion. Following the reanalysis of the Great Storm of October 1987 (Browning 2004), there has been a degree of focus on the sting jet phenomenon which can be responsible for very damaging winds in the dry slot. As described by Clark *et al.* (2005) and Hewson and Neu (2015), a sting jet (SJ) forms during the second stage of frontal fracture; the SJ then tends to be overtaken by the sometimes damaging winds associated with the low-level airstream coming around the bent-back front, known as the cold-conveyor-belt jet (CJ). The present paper, however, is concerned with neither a fully developed SJ nor the CJ; instead, it is about the shallow but vigorous boundary-layer convection that led to damaging winds in the dry slot at an even earlier stage, during the transition from an incipient frontal cyclone to the stage of frontal fracture.

We shall be making the case that this convection was not due directly to the potential instability caused by the very dry air of the DI overrunning the SMZ in the warm sector; rather, the boundary-layer convection was invigorated by a shallow stream of air sandwiched between the DI aloft and the underlying SMZ. We show that this airstream, later termed the Diabatically Modified Cloud-Top Layer (DMCTL), originated within an evaporating portion of a nearby belt of ana-cold frontal cloud. The importance of evaporative cooling in influencing the mesoscale dynamics of cyclonic weather systems has long been appreciated (*e.g.* Clough and Franks 1991; Thorpe and Clough 1991) but, by stimulating upright convection rather than slantwise convection, the manner in which it influences the weather is different in the present study.

The frontal cloud where the DMCTL formed in this study was part of an area that later developed into a cloud head (CH, as first defined by Böttger *et al.* 1975) but which for most of the time was still at the pre-CH stage. We develop the hypothesis that the substantial cooling and changes in potential vorticity associated with this evaporation may both have played a role in priming the boundary-layer convection that caused the damaging wind gusts. Of course the damaging surface winds would not have occurred had there not been very strong winds just above the boundary layer; however, this study does not address the origin of these strong winds but instead focuses on the convection that transported the high momentum to the surface.

2. The Model

The version of the WRF model used in this study was the Advanced Research WRF (ARW-WRF) 3.8.1 (Skamarock *et al.*, 2008). A 1-way nested configuration was employed with a large domain ('Domain 1') with 15 km grid spacing on a Lambert Conformal grid, covering much of the North Atlantic and European region and a nested 5 km domain ('Domain 2', 361×361 horizontal grid points, centred on the UK at 54 N, –4 W). The vertical grid had 48 levels (model top at 50 hPa) with a stretching function to give spacing of 120–240 m in the lower and mid-troposphere, with the lowest, full model level at 24 m above the terrain. The initialisation data were obtained from the ERA-Interim Reanalysis (Dee *et al.*, 2011). Both domains were initialised at 1800 UTC on 23 February 1997 and run for 36 hr. A pragmatic approach was adopted and a small number of test runs were conducted from which the combination of model physics schemes was selected which gave the best

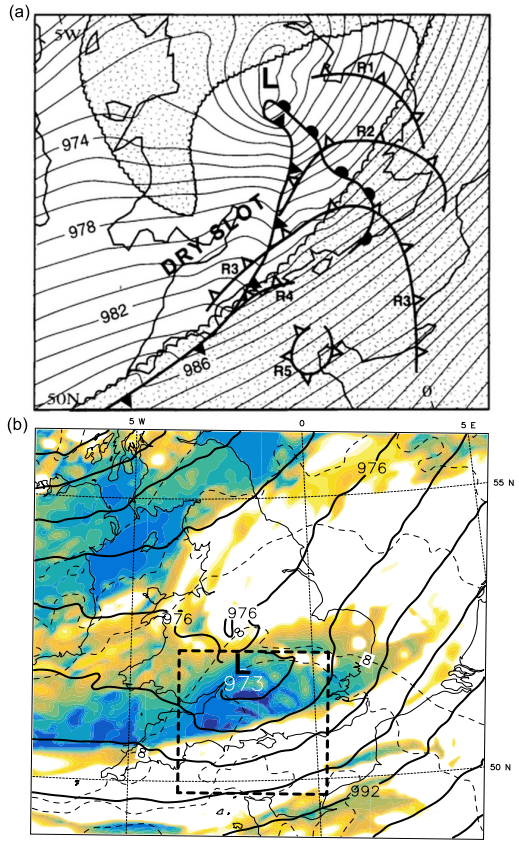

Figure 1. (a) Figure 12 from BR99– "Surface and frontal analysis for 2100 UTC 24 February 1997. Isobars are at 1 hPa intervals. Surface warm and cold fronts are plotted conventionally. Upper cold fronts associated with the arc rainbands (RI–R5) are shown with open symbols. The stippled area is added to show the extent of the cloud above the –15 C level". (b) Sub-section of model Domain 2 at 2100 UTC 24 February 1997. Model OLR shaded; SLP , solid contours every 4 hPa; θ_w at z= 1.5 km , dashed contours every 2 C. The area of Figure 3(a,b) is shown by the dashed box. This figure to be available in colour in the online article.

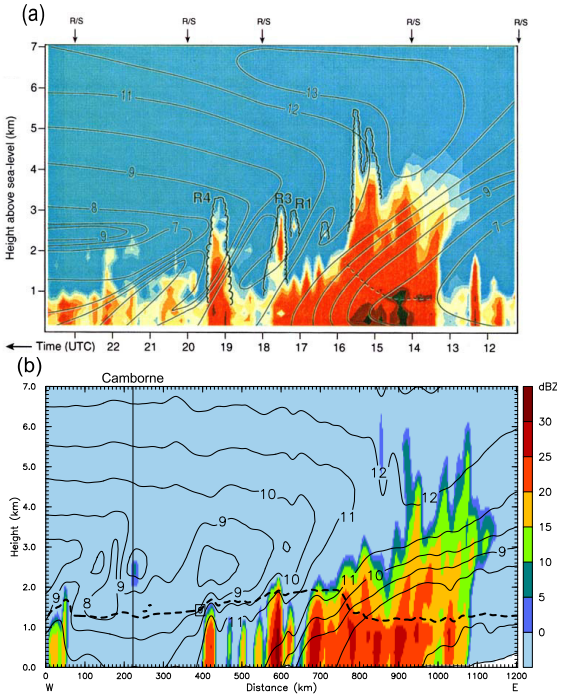

Figure 2. Comparison of model cross-section with UHF profiler and radiosonde observations from Camborne. (a) Figure 10(a) from BR99– "…isopleths of θ_w at 1 C intervals superimposed on radar received power (the large area of uniform blue shading corresponds to no detectable echo, and the areas of light blue through yellow, orange, red and brown represent increasing echo intensity, corresponding to moist boundary-layer air and or precipitation). Areas of precipitating convection are outlined by wavy lines, some of them corresponding to rainbands RI–R4. The black dashed line corresponds to the melting level as deduced from the UHF radar". (b) Cross-section of Domain 2 at 2100 UTC 24 February 1997 along the direction of travel of the system of convective rainbands. The distance scale in (b) is related to the time scale in (a) according to the system velocity. Model reflectivity (dBZ) shaded; θ_w, solid contours every 1 C; the dashed contour represents wet-bulb temperature = 0 C. The location of Camborne is indicated. This figure to be available in colour in the online article.

representation of shallow convection *in this case*, as judged by qualitative examination of model OLR (Outgoing Long-wave Radiation) and model-derived radar reflectivity fields.

The simulation reported here used a multi-scale version of the Kain-Fritsch cumulus scheme (MSKF only on Domain 1; no shallow or deep convection scheme was used on Domain 2), WSM5 (WRF Single-Moment 5-class) microphysics, RRTMG (Rapid Radiative Transfer Model for Global climate models) short-wave, RRTMG long-wave, YSU (Yonsei State University) planetary boundary layer, revised MM5 Monin-Obukhov surface layer and Noah land surface schemes. The reader is referred to Skamarock *et al.* (2008) for further details and references on the WRF parametrisation schemes.

Trajectory calculations were executed using the RIP (Read Interpolate Plot) post-processing package version 4 (Stoelinga, 2009) from 15-min WRF history files and interpolated at 5-min intervals to improve accuracy. A similar technique was used in the analysis of low-level jets within a rapidly developing cyclone by Smart and Browning (2013).

3. The case study

The results of this study are presented in five sections. The first section gives an overview of the event and some evidence of the broad validity of the model simulation by comparing it with observational analyses in BR99.

The other sections give detailed mesoscale analyses, beginning with a description in Section 3.2 of the atmosphere in the immediate vicinity of the convective rainbands, the vigour of which the study is trying to explain. Whilst diabatic cooling will be shown to be the underlying driver of the vigorous convection, we approach this issue indirectly in Section 3.3 by tracing the origin of air parcels ending up in a region of anomalously high potential vorticity found to cap the convection. In Section 3.4 we examine the changes in the properties of these parcels over the 9-hour period before they arrived in the region of the convection. Normally PV is considered to be of interest because it is a conservative property of adiabatic flows but in the present study it is of interest because changes of PV along these trajectories provide evidence of the evaporative cooling. Furthermore, the use of PV conveniently draws together what might seem to be disparate features relating to both the dynamics (*i.e.* vorticity) and the thermodynamics (*i.e.* static stability anomalies). Although a positive PV

anomaly itself should not be regarded as a mechanism capable of forcing convection within an underlying airmass, it does provide a useful indication that the basic forces and heat sources/sinks are such as to favour the underlying convection.

Finally, although the parcels analysed in the previous sections underwent substantial evaporative cooling, we continue in Section 3.5 by identifying nearby parcels that underwent as much or even greater evaporative cooling, finishing up at lower levels within the region of the convective rainbands and playing a major role in destabilising the boundary layer for convection.

3.1. *Overview of the convective rainband event*

The present simulation depicts the evolution and deepening rate of the observed storm fairly well. A surface analysis for 1200 24 February (all times are in UTC) shows a 976 hPa SLP centre near 50 N, –15 W, (see BR99 Figure 2(a)) whereas the new model run has a 983 hPa centre in the same position (not shown). By 0000 25 February the storm had deepened to 969 hPa with a centre over the east coast of England (BR99, Figure 1(b)) whereas the new model run has a 970 hPa centre located approximately 100 km to the south west.

Figure 1(a) in the present paper is a diagram from the original BR99 paper summarising the observations of the arc rainbands at 2100 on 24 February 1997. Using the words of BR99, *"viewed in action replay, the echoes [from the rainbands] are seen as a series of initially almost concentric arcs emanating from an 'epicentre' that travelled along the English Channel....."*. Figure 2(a), again from BR99, shows that these rainbands were due to shallow convection, as seen between 1700 and 1930 when the rainbands (labelled R1, R2... *etc*) passed over a site in south-west England. The figure is based on a sequence of radiosondes and continuous UHF radar profiles at Camborne. It shows that the rainbands were about 3 km deep and situated within a warm sector which was being overrun by air with low θ_w associated with a DI.

The DI created a dry slot between an elevated polar front cloud band to the south and an ana-cold frontal cloud band corresponding to an incipient cloud head (CH) to the north. The DI was laterally more extensive than the dry slot because part of the DI could not be seen from above where it was undercutting the polar-front cloud band. Parts of the arc rainbands extended into the region where the DI was undercutting the polar-front cloud. The observations in BR99 showed that the passage of an arc rainband was accompanied by a drop in temperature of up to 2 C, a small (0.5 hPa) jump in pressure and a 25 to 30° wind veer at the surface, consistent with the effect of convective downdraughts. The winds were mainly in excess of 40 m s^{-1} above 2 km (37 m s^{-1} at 1 km) and the rainbands travelled at 39 m s^{-1} (from 257°), and so it is not surprising that their downdraughts brought damaging wind gusts of up to 35 m s^{-1} to the surface.

Figure 1(b) shows that the new model does well at representing the incipient CH developing from the ana-cold frontal cloud band over central/northern England and Wales, with the dry slot and warm sector to the south of it. Moreover, it succeeds, where the previous modelling efforts of BR99 had failed, in reproducing a train of concentric arc-shaped cloud bands (in the 'dry slot', just north of the Isle of Wight). However, the bands do have a short wavelength of 25 km compared to an observed spacing four times as great and this casts some doubt as to whether the model is representing the physical mechanisms properly in all respects. Although the modelled arc rainbands in Figure 1(b) are partly obscured to the south by the higher-level polar-front cloud band, their true extent will be revealed by the more detailed mesoanalysis presented in Section 3.2.

Figure 2(b), shows the model-derived structure of the arc rainbands at 2100 within a vertical section along their direction of travel. The section passes through Camborne and the scale has been adjusted according to the travel velocity of the rainbands so that Figure 2(b) can be readily compared with the time-height plot of observations at Camborne in Figure 2(a). Convective showers in the warm sector corresponding to the arc rainbands can be seen between ranges 400 and 600 km. Farther east, the deeper and more extensive area of precipitation is associated with the warm front. With regard to the arc rainbands, the model gave tops at 2 km compared with 3 km for the observed convection, although in other sections shown later the model also gave tops to 3 km. There are more convective bands in Figure 2(b) than in 2(a), not only because of real differences between the simulation and reality, but also because not all of the observed rainbands actually passed over Camborne at the earlier time. Nevertheless, it is reassuring that the model was successful in reproducing a set of concentric arc rainbands emanating from a source over the English Channel.

3.2. *Mesoscale analysis of the convective rainbands*

We now take a closer look at the convective rainbands by zooming in on the area delineated by the dashed frame shown in Figure 1(b). This figure shows that the central and eastern parts of the area within the dashed frame, including the convective rainbands, are within the warm sector. Different aspects of the structure of the atmosphere within this region are shown by the plan views in Figures 3(a) and (b). The rainbands themselves are shown in Figure 3(a) by the thin black outlines representing a reflectivity of 20 dBZ: the arc rainbands are in the centre of the frame, the more extensive area of rain in the north being associated with the warm front and incipient CH. The arc clouds associated with the rainbands are shown by the shading representing cloud mixing ratio (cloud ice+cloud water).

The bold contours in Figure 3(a), depicting wind speeds of 44 m s^{-1} at a height of 1.5 km, show the strongest winds occurring in the vicinity of the convective arcs, particularly in the gaps between rainbands as noted in the severe windstorm described by Vaughan *et al.* (2015). These were regions of descent bringing down high momentum from above. The same wind-speed contours are also shown in Figure 3(b), together with information about the potential vorticity: the shading represents PV>2 PVU (PV Units) at 1.5 km and the dashed contour represents the extent of PV>2 PVU at 2 km. The belt of high PV at both 1.5 and 2 km in the northern part of the figure was, as we show

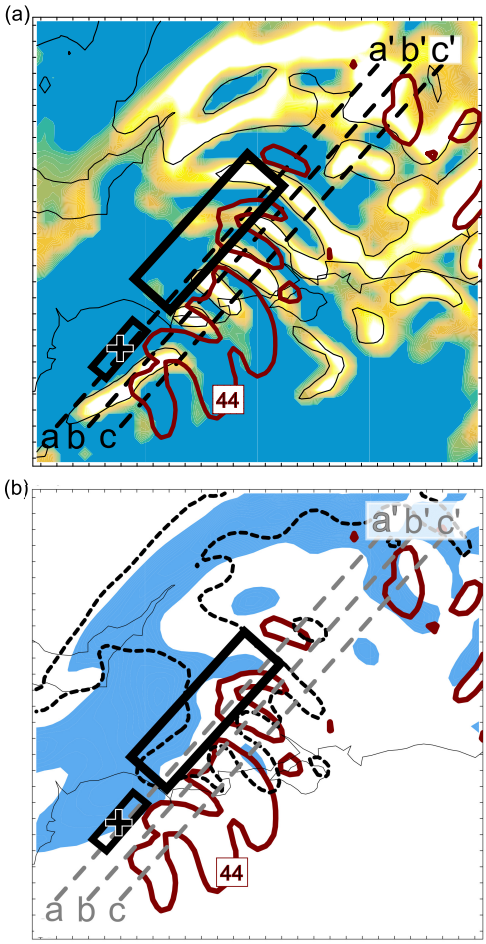

Figure 3. Sub-section of Domain 2 at 2100 UTC 24 February 1997. (a) Cloud mixing ratio (ice+water) shaded, white >0.5 g kg^{-1}; model-derived column maximum reflectivity, fine contour 20 dBZ; horizontal windspeed at z = 1.5 km, bold contour 44 m s^{-1}. (b) Potential vorticity at z = 1.5 km greater than 2 PVU shaded; potential vorticity at z = 2.0 km dashed contour 2 PVU; windspeed bold contour 44 m s^{-1}. The locations where two sets of trajectory parcels were initialised (see text) is indicated by the rectangular boxes and **+**. The parcels within the long rectangular box are later referred to as A-parcels and those in the smaller box with the **+** are referred to as B-parcels. The locations of the three cross-sections, aa′, bb′ and cc′, in Figure 4 are indicated by the dashed lines. Each sub-section is 280×280 km, tic marks are every 10 km. This figure to be available in colour in the online article.

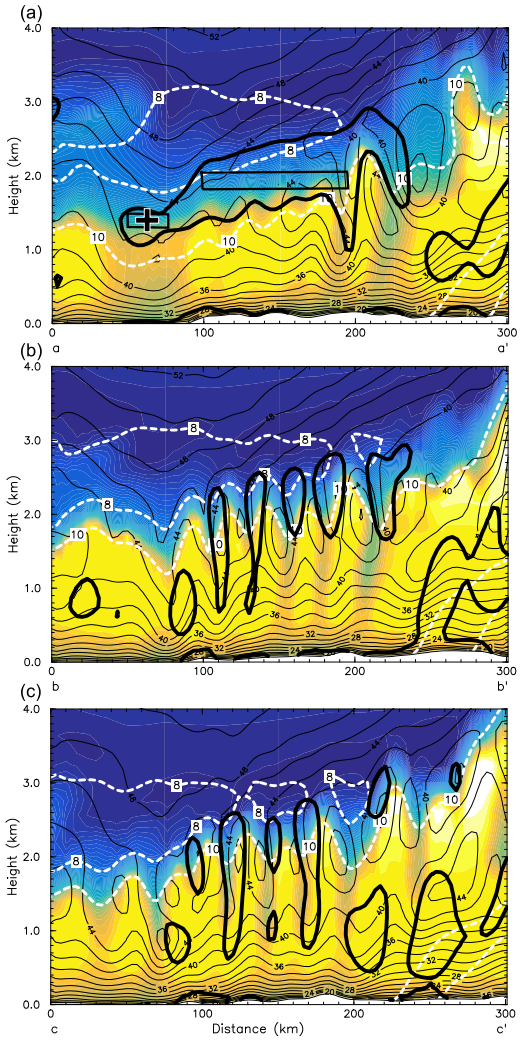

Figure 4. Cross-sections from Domain 2 at 2100 UTC 24 February 1997 along (a) aa′, (b) bb′ and (c) cc′ in Figure 3. Relative humidity shaded from 70% (dark) to 100% (light) in 5% increments; horizontal windspeed black contours every 2 m s^{-1}; Potential vorticity bold, black contour 2 PVU; θ_w, white dashed contours at 8, 10 and 12 C.The locations where two sets of trajectory parcels were initialised (see text) is indicated by the rectangular boxes and **+**. Air parcels within the larger rectangle are referred to in the text as A-parcels and those in the small rectangle with a **+** are referred to as B-parcels.This figure to be available in colour in the online article.

later, generated diabatically within the region of cold-frontal ascent associated with the incipient CH. Significantly, a large area of high PV also extends southwards at these levels towards the convective rainbands within the 'dry slot'. Although most of this high PV is on the north-western, *i.e.* upstream, edge of the rainbands, fingers of high PV do extend some way into the gaps between the rainbands, especially at 2 km: essentially the convection was lifting air with lower PV into the air characterised by the higher PV. Whereas some of the high PV in northern parts of the figure was generated by condensation heating, we shall show later that the high PV in the vicinity of the rainbands was generated by evaporative cooling.

The detailed vertical structure of the rainband environment is depicted in the cross-sections in Figures 4(a,b,c), taken along the dashed lines aa′, bb′ and cc′ in Figure 3. The convective clouds responsible for the arc rainbands were shallow: as shown by the distribution of relative humidity (shading), they varied in depth from almost 2 to 3 km.

The tops of the convective clouds are roughly defined in Figure 4 by the 10 C θ_w contour (dashed white lines). Above the convection there is very dry air (darker shading), with θ_w as low as 8 C, associated with the DI. Sandwiched between the driest air and the convection, however, there is a layer of intermediate humidity (medium shading) associated with air characterised by PV= 2 PVU, as shown by the bold line in Figure 4(a). We saw in Figure 3(b) that fingers of this high PV intruded in between the convective rainbands, or, alternatively, the convection intruded into the layer of high PV, and these intrusions can be clearly seen in Figures 4 (b and c). We show later that these patches of high PV had reached this location after descending through a kilometre or so and experiencing evaporative cooling; they are distinct from some other patches of high PV at lower levels in Figure 4, especially those beyond range 230 km, close to

the cold-frontal zone, which were being created locally by condensation in the frontal ascent.

The thin lines in Figure 4 are isotachs of wind speed. These show high wind speeds in the DI, with values in excess of 40 m s^{-1} extending down into the boundary layer in the region of the convection. Indeed there is evidence of a broad low-level jet (LLJ), with multiple maxima between 44 and 48 m s^{-1} at heights of between 900 and 2000 m, apparently broken up by fingers of lower wind speed due to the penetrating convective clouds. The presumption is that the convection was assisting the downward transport of the high momentum and hence was responsible for the damaging surface wind gusts encountered on this occasion. The goal of this study is to investigate the mechanisms that may have enhanced the vigour of this convection.

3.3. Origin of the air with high PV that overran the convective rainbands

We have identified a positive PV anomaly in the vicinity of the convective rainbands, centred near a height of 2 km. The anomaly in this region was roughly 1 km deep and 100 to 150 km wide at 2100. In this section we trace the origin of this anomaly. To do this we have used the 5-km grid model to calculate trajectories of air parcels starting within the PV anomaly in the vicinity of the convective rainbands in positions shown by the small rectangles drawn in Figures 3 and 4. One set of parcels, designated the A-parcels, was started in the larger rectangle in the aa′ section at a height of 2 km, close to the convective tops and on their upstream side. The other set of trajectories, associated with the so-called B-parcels, was started in the smaller rectangle identified by a + marker at a height of 1.4 km, in the region where the PV anomaly attained its lowest penetration within the aa′ section. We have produced two corresponding sets of trajectories, both starting at the time shown in Figures 3 and 4: trajectories were calculated backwards to 1500 24 February and forwards to 2400. Other sets of trajectories were also derived using the model run with a 15-km grid to extend these trajectories to cover the period 0600/24th to 0600/25th of February. These were used to reveal the locations of the parcels at 1200 but were otherwise not used in the subsequent more detailed analyses. Trajectory and parcel properties were largely consistent between the 5- and 15-km grids despite the difference in effective resolution.

In this section we shall show the location of the sets of parcels at 4 times, (1200, 1500, 1800 and 2100), using plan plots (Figure 5), vertical cross-sections (Figure 6) and tephigram profiles (Figure 7) taken through the centre of the A-parcel array at each time; the same profiles were also used to study the B-parcels which, although not collocated with the A-parcels, were fairly close by (see the + markers in Figures 5 and 6). The cluster of A-parcels remained fairly compact over the period of study, being contained within the rectangles drawn in Figures 5 and 6; the cluster of B-parcels remained similarly compact.

Before focusing on the parcels themselves, we start by noting the evolution of the incipient cyclone system within which the parcels were travelling. Figure 5(a–d) shows a low-pressure centre of 980 to 981 hPa at 1200 and 1500 which then deepens at an average rate of 1 hPa hr^{-1} over the subsequent 6-hour period to 2100. The bold contours, depicting θ_w at 0.5 km, show a warm sector situated to the south of the low-pressure centre. The warm sector was characterised by a SMZ, the top of which lay just beneath the position of the parcels at 2100. At this, still early, stage in the development of the cyclone, there is rather little evidence of the frontal fracture that started soon after 2100.

The cloud pattern, as represented by the OLR, shows three main west-east orientated features which are labelled in Figure 5(b) and can be seen in the subsequent panels as the system travelled eastwards towards and across the British Isles. The mass of cloud to the south is the polar-front cloud band (PFCB) associated with an upper cold front. The cloud band to the north is an ana-cold frontal cloud band (ACFCB) which we show later was characterized by air ascending slantwise with a component towards the north. Between these two cloud bands is the dry slot, produced by the very dry air of the DI which was overrunning the ACFCB to the north and undercutting the elevated PFCB to the south. The relationship between the PFCB and the ACFCB can be understood in terms of the split cold-front model (Browning and Monk,1982) in the following way. The PFCB corresponds to the upper cold front at the leading edge of the overrunning DI, and the ACFCB corresponds to the surface cold front. In the usual depiction of the split cold-front model, the surface cold front is a shallow kata-cold front, but in a study of one such front that later evolved into a cloud head, Browning (1995) showed that the shallow surface front in a split-front situation can begin to develop into an ana-cold front with an initially shallow rearward slantwise circulation which might deepen over time. This is what happened on the present occasion.

The rectangular boxes and large crosses in Figures 5(a-d), depict the locations of the A- and B-parcels, respectively: the A-parcels are distributed throughout the area of each box and the B-parcels are all within a radius of 20 km centred on each cross. All of these parcels are seen to have been within or close to the dry slot. They were near the southern edge of the ACFCB and close to or partly beneath the elevated PFCB that extends west-to-east to the south of the parcels. The position of the parcels with respect to these cloud features will become clearer when we look at vertical cross-sections along the dashed lines in Figure 5.

The cross-sections in Figures 6(a–d) are all south-north sections taken through the centre of the set of A-parcels as they travelled roughly from west to east. Thus they represent the evolving environment of the parcels as they travel through the system rather than giving a true indication of the evolution of the overall system. The sections at all four times show regions of high humidity associated with the cloud features mentioned previously. On the far left is the elevated PFCB and just right of centre is the ACFCB that began to evolve into a CH by 2100. Between the two is the DI bringing down dry air with low θ_w. Strictly, the dry air with low θ_w extends on both sides of the ACFCB and so the latter can be regarded as being a slantwise extrusion of boundary-layer air into the cold dry air. At 1200 Figure 6(a) shows a tongue of air with a θ_w of 10 C ascending within the cloud sheath of the ACFCB; at later times the θ_w in the

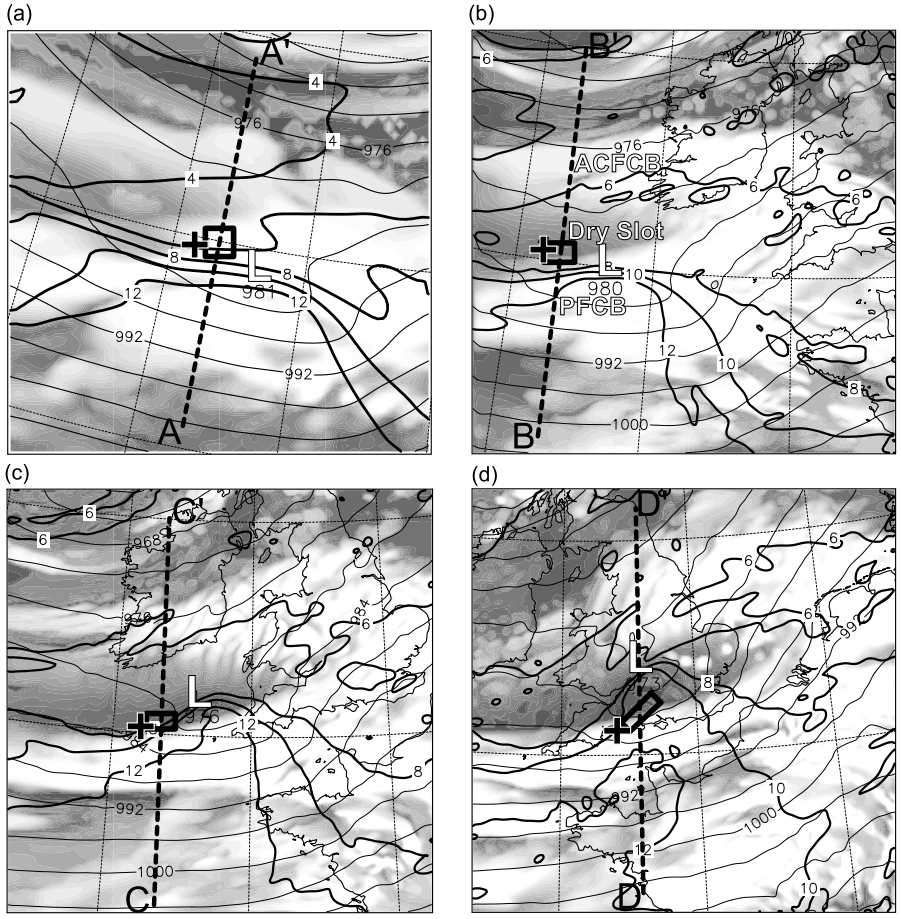

Figure 5. Sub-sections of Domain 2 at (a) 12, (b) 15, (c) 18, (d) 2100 UTC 24 February 1997. OLR shaded; SLP, solid contours every 4 hPa; θ_w at z=0.5 km, bold contours every 2 C. The locations of the sets of trajectory parcels at each time are indicated by the rectangular boxes (A-parcels) and + (B-parcels). The locations of the cross-sections in Figure 6 (see text) are indicated by the dashed lines which pass through the centroid of the parcel clusters at each time. The location of the SLP centre is labelled with L and the locations of the dry slot, ana-cold frontal cloud band (ACFCB) and polar front cloud band (PFCB) are labelled in (b). Each sub-section is 1100×1100 km.

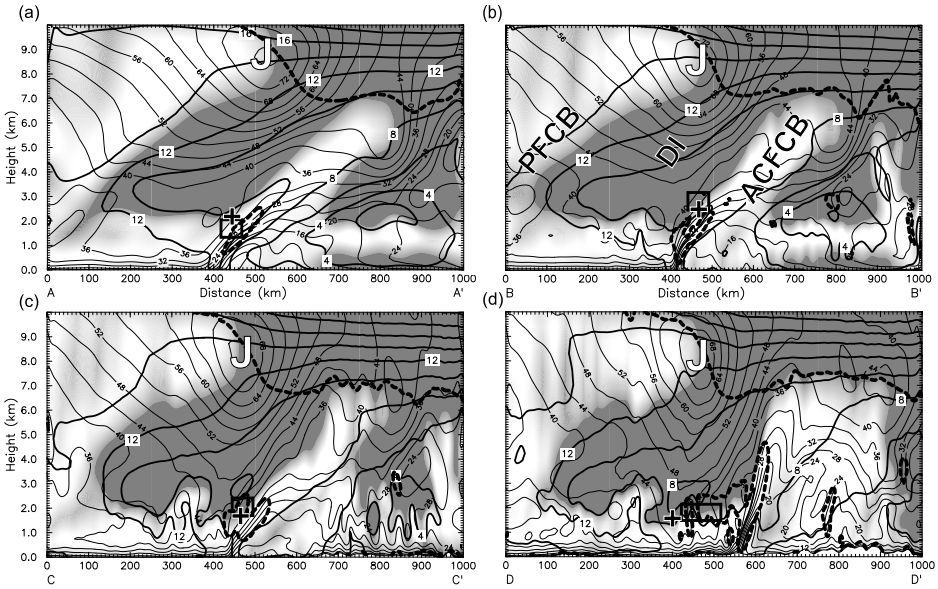

Figure 6. Cross-sections in Domain 2 at (a) AA′, 1200 UTC (b) BB′, 1500 UTC (c) CC′, 1800 UTC and (d) DD′, 2100 UTC 24 February 1997. Relative humidity w.r.t. ice shaded from 70% (gray) to 100% (white); horizontal windspeed black contours every 2 m s^{-1}; potential vorticity bold, dashed contour 2 PVU; θ_w every 2 C black, bold contours. The locations of the sets of trajectory parcels at each time are indicated by the rectangular boxes (A-parcels) and + (B-parcels). The axis of the upper jet J, the ana-cold frontal cloud band (ACFCB), the dry intrusion (DI) and the polar front cloud band (PFCB) are labelled.

cloud sheath decreases to 9 C and the θ_w-maximum is not explicitly resolved by the simplified contouring used here.

The dashed contours in Figure 6, depicting a potential vorticity of 2 PVU, show two categories of high PV. One corresponds to stratospheric air. The tropopause is seen to lower by 3 km in the region of a upper-level jet, with winds in excess of 70 $\mathrm{m\,s^{-1}}$, but there is not a deeply penetrating fold at this stage. The other category of high PV corresponds to diabatically generated PV. The main source of such PV is at low levels due to condensation within the ACFCB. As time goes by, the extent of the diabatically generated PV increases. By 2100 a finger of high PV is beginning to extend upwards towards the tropopause. At the same time Figure 6(d) shows that an area of high PV also extends southwards into a position just above the SMZ in the warm sector where, as shown in Figures 3 and 4, it was associated with the convective rainbands: this is the PV anomaly that we are primarily concerned with in this study. We shall shortly show that the part of the PV anomaly that extended southwards was due to evaporative cooling in part of the ACFCB. For the present it suffices to note the slight evidence of a splitting of the PV anomaly in Figures 6 (b) and (c). The splitting is an important feature but is only marginally resolved in these figures: later more detailed analyses (Figures 11(a) and (b)) show it to be a well defined feature.

The small rectangles and + markers in Figures 6(a–d) show that the A- and B-parcels are within the cloud deck of the ACFCB and near or above the upper edge of the condensationally-generated PV at 1200 (Figure 6(a)) but, by 1800 (Figure 6(c)), they are just above the cloud deck and associated with the upper limb of the split PV which we shall shortly be attributing to the evaporation of part of the cloud deck. By 2100, Figure 6(d) shows that the parcels have descended into the southward extension of the PV anomaly from their position just above the cloud deck to a position above the SMZ in the warm sector where the convective rainbands were occurring.

The vertical location of the parcels in relation to the ACFCB cloud deck is shown in more detail by the sequence of tephigram profiles in Figure 7(a–d). The tephigrams have been derived for locations passing through the midpoint of the cluster of A-parcels at 1200, 1500 1800 and 2100. The black and grey arrows show the heights of the A- and B-parcels, respectively, but we restrict the following description to just the A-parcels:

At 1200 Figure 7(a) shows the A-parcels at 780 hPa within the cloud layer. They are in the saturated core of the ana-cold frontal ascent and have a θ_w of just over 10 C. Below the parcels, there is a deep frontal zone with a stable layer extending from 800 down to 900 hPa.

By 1500 (Figure 7(b)), the parcels have ascended to 690 hPa. During the 3 hours up to 1500, the top of the cloud layer had been eroded by mixing with the overlying DI air and by evaporation. The parcels at 1500 are situated close to the new cloud boundary, with their θ_w reduced to just below 10 C and with a relative humidity just beginning to decrease below 100%.

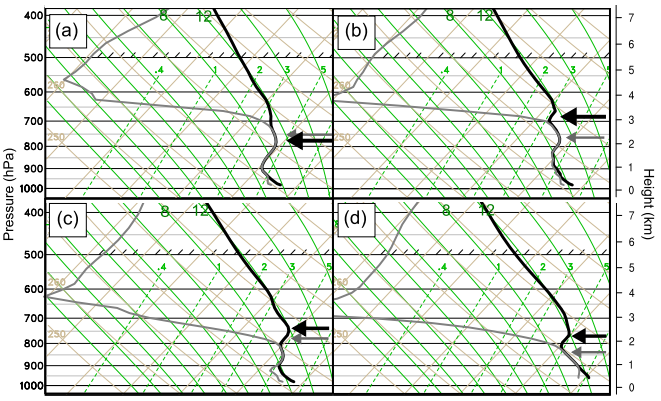

Figure 7. Sequence of model-derived tephigrams derived for locations of A-parcels at (a) 1200, (b) 1500, (c) 1800 and (d) 2100 UTC 24 February 1997. Dry-bulb temperature (black curve) and dew-point (grey curve). The black and grey arrows show the heights of the A- and B- parcels, respectively

By 1800 (Figure 7(c)), the parcels have descended slantwise just above the top of the ACFCB cloud layer to reach the 740-hPa level. In doing so, their relative humidity has decreased substantially and their θ_w has diminished to 9 C as they mixed with the DI air. As a result of adiabatic warming, the parcels are now at the top of a stable layer capping the cloud layer.

By 2100 (Figure 7(d)), the parcels have descended further, to 770 hPa. In travelling southwards relative to the system, they are now located above the unstable SMZ which characterises the warm sector close to the cold front.

Although the evaporative cooling of the A- and B-parcels makes a contribution to the invigoration of the boundary-layer convection, we shall argue that there were other factors that are likely to have been more important in intensifying the convective instability. One factor was the comparable or even greater evaporative cooling that occurred in some nearby parcels that descended to lower levels in the region of the convective rainbands: this is discussed in Section 3.5. The other factor is the development of the PV anomaly itself within the airstream characterised by these A- and B-parcels.

3.4. Changes in the properties of the air parcels with high PV that overran the convective rainbands

In the previous section we traced the location of sets of air parcels over a 9-hour period, up to the time when they arrived in a position near the top of the convective rainbands with a positive PV anomaly. We now describe the evolution of various properties of these parcels over this period and, in particular, show how the development of the PV anomaly within these parcels was linked to evaporative cooling.

Figure 8 shows the variation in various properties of the A- and B-parcels during the period from 1200 to 2100 when they arrived in the region of the convective

rainbands (solid curves) and for 3 hours afterwards (dashed curves). The black curves represent the average values for the 20 A-parcels initialised within the rectangles in Figures 3 to 6, and the grey curves represent the averages for the 4 B-parcels initialised near the + markers in these figures*. Both sets of parcels originated in the ACFCB and underwent a similar descent of about 1 km over about 5 hours before arriving in the region of the convective rainbands. Prior to that, trajectories derived using the 15-km-grid model run over a larger domain (not shown) revealed that the parcels had risen from lower levels as part of the cold-frontal slantwise ascent on the warm side of a trailing baroclinic zone over the western and central Atlantic Ocean. During their descent, at up to 10 cm s^{-1}, the parcels accelerated from 30 to over 40 m s^{-1} and, following the total evaporation of the cloud, their relative humidity dropped to around 60%.

The evaporation led to substantial cooling, *i.e.* reduction in θ. At the same time as the θ of the parcels decreased by 2 to 3 C, the θ_w of the parcels decreased by a little over 1 C. The decrease in θ_w will have been due to mixing of the cloudy air with the overlying DI which was characterised by low values of θ_w. Although the air in the DI was colder than the underlying cloudy air in terms of θ_w, it was warmer in terms of θ, so that, had it not been for the mixing, the decrease in θ due to evaporative cooling would have been even greater.

Figure 8(c) shows the variation of moist potential vorticity. Following Gray *et al.* (2011), we use MPV*, which is the moist potential vorticity calculated using saturated θ_e instead of simply using θ_e (where θ_e is equivalent potential temperature). The MPV* of the A- and B-parcels remained positive throughout (Figure 8(c)), suggesting that conditional symmetric instability (CSI) was not playing a role except possibly prior to and at the beginning of their descent when MPV* was near zero.

Figure 8(f) shows the variation of dry potential vorticity. This increased fairly consistently from about 1 to 3 PVU during the main 3-hour period of descent. Although the PV of the B-parcels decreased after 2000, that of the A-parcels continued increasing, reaching 3.5 PVU by the time they were just above the convective rainbands, after which they too experienced a decrease in PV as they encountered the convection. As we shall explain, the generation of the positive PV anomaly was due to the evaporative cooling.

Quantitative support for the existence of a link between evaporative cooling and the generation of PV is provided by Figure 9. Figure 9(a) shows a zoomed-in portion of the cross-section for 1500 depicted in Figure 6(b). It shows potential vorticity, with contours for 1, 1.5 and 2 PVU, superimposed on the sloping cloud layer associated with the ACFCB (light shading representing high relative humidity) which was being generated by the slantwise ascent of air with θ_w of from 9 to 10 C at this time (thin contours). Figures 9(b) and (c), respectively, show the corresponding patterns of the 2-hour increments in θ and PV as an approximation to the material rates of change of these

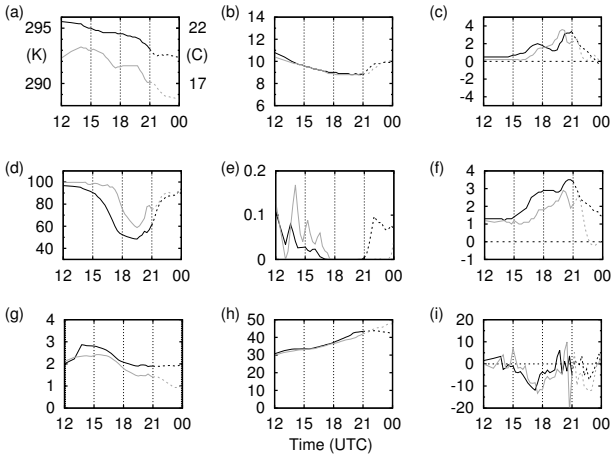

Figure 8. The mean properties of the A- and B- parcels (black and grey curves respectively) during the period from 1200 to 2100 UTC when they arrived in the region of the convective rainbands (solid curves) and for 3 hours afterwards (dashed curves). (a) θ (K) left axis, (C) right axis; (b) θ_w (C); (c) moist potential vorticity MPV* (PVU); (d) relative humidity w.r.t. ice (%); (e) cloud mixing ratio (cloud water + cloud ice) (g kg^{-1}); (f) dry potential vorticity (PVU); (g) height (km); (h) horizontal windspeed (m s^{-1}); (i) vertical velocity (cm s^{-1})

variables. These are superimposed on the pattern of relative humidity as plotted in (a). The 2-hour increments have been derived from parcel trajectories, taken forwards and backwards by one hour from positions spaced at intervals of 20 km horizontally and 200 m vertically throughout the domain covered by the figure. Also shown in each of the three panels are the positions of the A- and B-parcels, (together with the positions of C- and D-parcels which are discussed in the next section).

The most notable feature of Figure 9(a) is the splitting in the distribution of PV. This was mentioned earlier in connection with Figure 6 but is much clearer in this enlarged view. As we shall explain, the split layer of PV provides evidence for the role of the evaporation in creating part of the positive PV anomaly (*i.e.* the upper layer in the split PV pattern) that was subsequently advected into the region of the convective rainbands.

The distribution of the 2-hour θ change, shown in Figure 9(b), is a measure of the diabatic heating which, although affected by mixing, as mentioned above, was dominated by latent heating and cooling. The pattern of heating/cooling is seen to be characterised by three sloping layers associated with the ACFCB. The solid contours within the ACFCB enclose the main strip of condensational heating, with 2-hour changes of over 3 C occurring over a depth of 600 m. Beneath this there is a layer of cooling associated with evaporation (and sublimation) in the cold air descending below the frontal zone. Above the layer of condensational heating there is another sloping layer of cooling associated with evaporation of the cloud top, especially at ranges 70 to 150 km. The cooling would have been due to evaporation of cloud rather than precipitation because, according to the model, the concentration of precipitation was negligible in this region. Part of the evaporative cooling at cloud top will have been due to ice sublimation. The concentration of cloud ice was comparable to that of the cloud liquid water:

*Increasing the number and density of the trajectories did not substantially change the results.

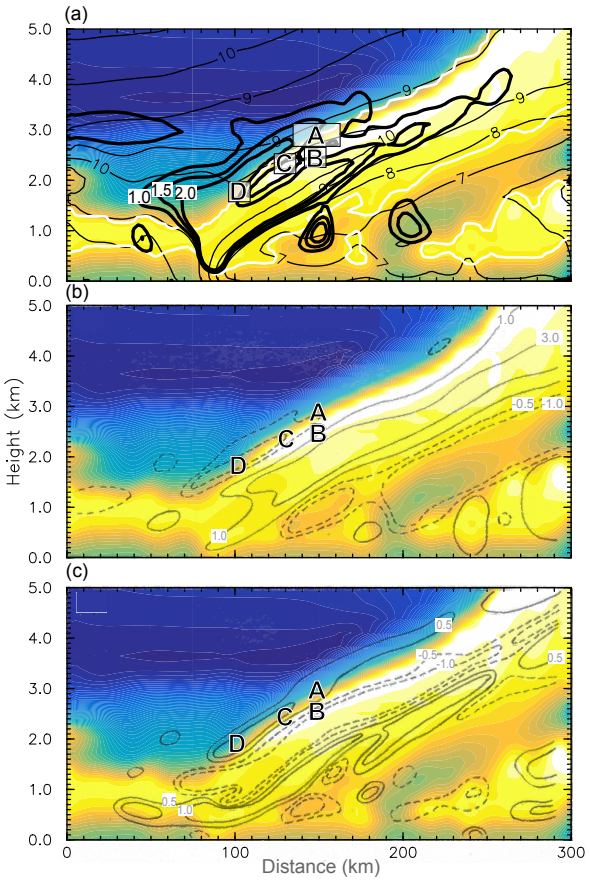

Figure 9. South–north cross-sections along BB′ in Figure 5(b) demonstrating the link between evaporative cooling and the generation of PV, showing a zoomed-in portion of the cross-section for 1500 UTC depicted in Figure 6(b). (a) Potential vorticity bold, black contours for 1, 1.5 and 2 PVU; relative humidity w.r.t. ice shaded from 30% (dark) to 110% (light) in 5% increments and bold, white contour 99%; θ_w thin contours every 1 C. (b) Relative humidity w.r.t. ice shaded and 2-hour increments in θ, thin contours with negative increments shown dashed (contours for 1.0 and 3.0, and for –0.5 and –1.0 C). (c) Relative humidity w.r.t. ice shaded and 2-hour increments in potential vorticity, thin contours, negative increments are dashed (contours for 0.5 and 1.0, and for –0.5 and –1.0 PVU) . The incremental changes in θ and potential vorticity were computed from the trajectory diagnostic history files and plotted manually. The locations of the A-, B-, C- and D- parcels are indicated, (the C- and D-parcels are explained later, in Section 3.5). This figure to be available in colour in the online article.

about 0.02 g kg^{-1} for the A-parcels and about twice that for the B-parcels at 1500, before dropping to zero by 1800.

The three sloping layers of heating/cooling are seen in Figure 9(c) to be associated with three coherent layers of increasing and decreasing PV: a layer of decreasing PV is situated just above the sloping layer of condensational heating, the underlying layer of increasing PV is situated just below the layer of condensational heating, and the uppermost layer of increasing PV is situated just above the topmost layer of evaporative cooling.

Figure 10 is a schematic that explains the relationship between PV generation and the heat sources and sinks due to phase changes. Strictly, semi-geostrophic theory, applicable to a quasi two-dimensional front, states that the PV tendency should be orientated along absolute momentum (M) surfaces. In frontal regions the isentropic surfaces are sloping and the momentum surfaces are not vertically orientated. This might be construed as invalidating the simple interpretation sketched in Figure 10. However, Figure 9 shows that the front is only modestly inclined (less than 1 in 60) in the vicinity of the A- and B-parcels, and so the assumption of quasi-vertically orientated PV tendencies is reasonably good and Figure 10 is a useful approximation (pers. comm. A. Thorpe).

As shown by the position of the parcels in Figure 9, it can be seen that the schematic is representative of the region where the PV was split. The left-hand profile in Figure 10 shows the condensational heat source (+) associated with the frontal cloud layer and the evaporative heat sink (–) associated with the layer above where the cloud is evaporating (for simplicity we do not represent the evaporation at the base of the cloud). Diabatic changes in potential vorticity are achieved through changes in the static stability. Thus, just above the heat sink (–), and also just below the heat source (+), there are increases in PV owing to increasing stability[†]. However, in between, where a heat sink is above the heat source, there is a reduction in PV owing to decreasing stability, thereby accounting for the split pattern of PV. The parcels that are the focus of this study and later advected into the region of the convective rainbands, were associated with the upper limb of the split pattern, *i.e.* with the evaporation. We refer to the twin layers of evaporative cooling and associated PV generation at the top of the cloud deck collectively as the *diabatically modified cloud-top layer*, or DMCTL.

The A-parcels discussed earlier were situated close to the region of cloud-top evaporative cooling and PV generation at 1500 (Figure 9) and, according to Figure 8, at subsequent times there was a protracted period of cooling and increasing PV. (The B-parcels were just below the layers of cooling and PV generation at 1500 but, according to Figure 8, started cooling and increasing their PV soon after.) Thus the evaporatively induced positive PV anomaly intensified as the associated airflow carried it down towards the warm sector where the convective rainbands were triggered. This slumping down of the upper limb of the split PV pattern can be seen in Figure 11 which shows the A- and B-parcels associated with the upper limb finishing up just above the shallow layer of high θ_w in the warm sector as previously shown in Section 3.2.

3.5. *Evolution of parcels that were affected by strong evaporative cooling and descended to very low levels in the region of the convective rainbands*

In order to examine the history of the air experiencing some of the strongest cooling, and which descended to particularly low levels in the region of the convective rainbands, we have defined two clusters of what we shall call the C- and D-parcels, as labelled in Figures 9 and 11. We have calculated the back trajectories of these parcels from 1500 to 1200 and their forward trajectories from 1500 to 0000 on 25 February. The time histories of their properties are plotted in Figure 12. This figure shows that the C- and D-parcels spent more of their time within

[†]In practice, vertical advection may raise or lower the PV anomaly somewhat above its source region.

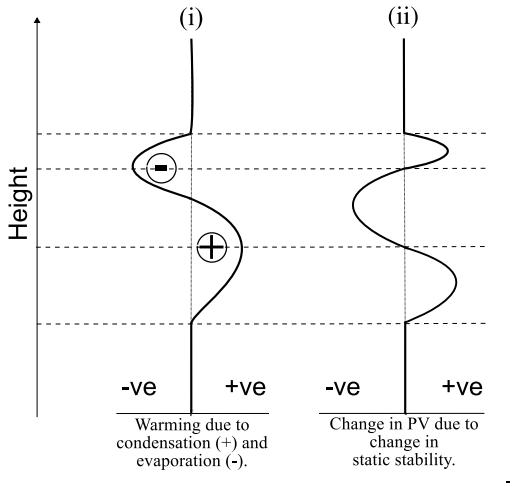

Figure 10. The relationship between (i) heat sources and sinks due to phase changes of water and (ii) the resulting generation of potential vorticity.

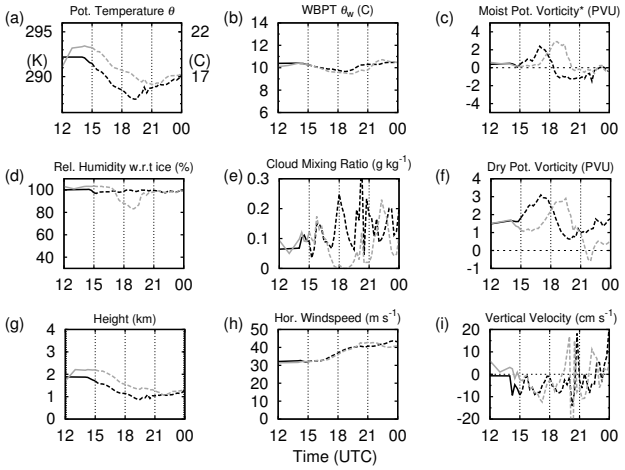

Figure 12. The mean properties of the C- and D- parcels (black and grey curves respectively) which experienced the strongest cooling. Mean properties of backward trajectories for the period from 1200 to 1500 (solid curves) and forward trajectories for 9 hours from 1500 (dashed curves). (a) θ (K) left axis, (C) right axis; (b) θ_w (C); (c) moist potential vorticity MPV* (PVU); (d) relative humidity w.r.t. ice (%); (e) cloud mixing ratio (cloud water + cloud ice) (g kg^{-1}); (f) dry potential vorticity (PVU); (g) height (km); (h) horizontal windspeed (m s^{-1}); (i) vertical velocity (cm s^{-1}).

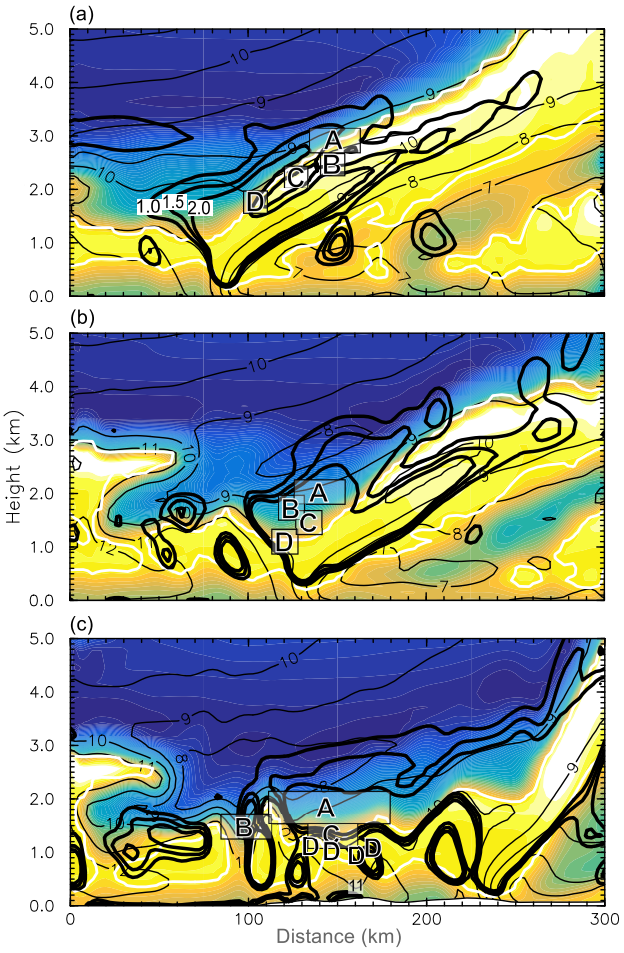

Figure 11. South–north cross-sections through the locations of the A-, B-, C- and D- parcels at (a) 1500, (b) 1800 and (c) 2100. Relative humidity w.r.t. ice shaded from 30% (dark) to 110% (light) in increments of 5% and bold, white contour at 99%; potential vorticity bold, black contours for 1, 1.5 and 2 PVU; θ_w thin contours every 1 C. The locations of the A-, B-, C- and D-parcels are indicated; the boxes indicate the approximate envelopes of the A- and B-parcels. This figure to be available in colour in the online article.

the cold-frontal cloud than the A- and B-parcels, during which time their rate of cooling was particularly large. Whereas the A- and B-parcels attained low values of relative humidity as they descended and mixed with the very dry air of the DI, the C- and D-parcels (especially the C-parcels) remained close to saturation (and a vertical shear of 5 m s^{-1} over the 400 m), with a large cloud mixing ratio. This indicates a state of equilibrium in which the reduction in relative humidity that would have resulted from their descent was being balanced by an increase in humidity due to evaporation. This state of equilibrium prevailed for about 5 hours during which the parcels descended by about 1000 m. In order to sustain such evaporation, cloud and/or precipitation must somehow have continued to form within or enter this region throughout this period. Cloud forming in situ, perhaps due to embedded small-scale eddies, can be dismissed since it would have produced a heat source that would have counteracted the evaporative cooling. Cloud and precipitation could not have entered this region from above because it was capped by the DI. That leaves the possibility that small eddies associated with the strong vertical wind shear and locally reduced static stability were lofting cloud particles into the region from the underlying layer of frontal ascent.

For the 5-hour period during which the C- and D-parcels were descending, their potential temperature dropped by as much as 4 to 5 C. As in the case of the A- and B-parcels discussed above, the cloud ice concentration was comparable to that of the cloud liquid water, with values of typically 0.01 to 0.03 g kg^{-1} until 1700 or 1800, and so a contribution to the cooling would have been due to ice sublimation as well as to evaporation of cloud water. The C-parcels continued to contain cloud and to cool diabatically as they continued descending between 1800 to 1900, by

which time all of the cloud ice had melted, and so a contribution to the cooling would have been due to melting.

During the 5-hour period of descent, the height of the C- and D-parcels decreased from about 2 km down to as low as 1 km when they reached the area of the convective rainbands. This height was significantly lower than that reached by the A- and B-parcels that produced the layer of high PV blanketing the convective rainbands. This large degree of cooling of air penetrating to so low a level above the SMZ would have had a major effect in invigorating the convection. The potential vorticity of the C- and D-parcels also increased as they descended, reaching 3 PVU, as for the A- and B-parcels, but their PV decreased later as the parcels encountered underlying frictional effects within the boundary layer and diabatic heat sources owing to the very convection that they were helping to stimulate.

4. Discussion

What do the above results tell us about the processes responsible for the damaging winds as this storm crossed the UK? The earlier study of this case by BR99 showed that strong winds were brought down to the lower troposphere and that bands of shallow but vigorous boundary-layer convection transported the high momentum to the surface. The two questions needing to be addressed are– (i) what factors were involved in creating the strong winds at the top of the boundary layer? (ii) What factors accounted for the vigour of the boundary-layer convection? The present study addresses only the second of these questions. However, before going on to discuss our answers to the second question, it is appropriate to make a few remarks about the first question.

Strong winds in dry intrusions, as in this study, are common. There is evidence in the present case of a low-level jet (LLJ) near the top of the boundary layer. Although broken up into multiple maxima by the penetration of convective cells, Figure 4 shows a maximum speed in the LLJ of over 44 $\mathrm{m\,s^{-1}}$. The maximum occurred at heights mainly close to 2000 m, but as low as 900 m in one place (*i.e.* range 70 km in Figure 4(c)) where the dry air seems to be penetrating particularly deeply into the boundary layer. This LLJ is somewhat reminiscent of a sting jet as described by Smart and Browning (2014) but it did not exhibit the spatially extensive coherence that Smart and Browning found to be a feature of SJs. Moreover, the present study was for the period before and during the transition from an incipient cyclone to the frontal-fracture stage and according to Hewson and Neu (2015), who studied many such storms, SJs tend not to develop until frontal fracture is well underway. Nevertheless we do not rule out the possibility that the present LLJ may have been generated by the same factors as a SJ. Recent studies are pointing to the important role of flow down the pressure gradient in generating the strongly descending and accelerating flow that becomes a SJ (Coronel *et al.* 2016; Slater *et al.* 2015). These same studies show that such forcing can generate the strong winds and descent without the need to invoke diabatic effects. If the same applies to the LLJ in the present study, then the evaporative cooling would more likely have been the result rather than the cause of the descending LLJ. However, the dynamical geostrophic forcing by itself is often insufficient to enable the high momentum to be transported efficiently through the boundary-layer, and this is why the evaporative cooling becomes important.

This leads us to the main point of the present case study: to demonstrate in detail the ways in which evaporation stimulated convection that led to the transport of the high momentum to the surface. Slater *et al.* (2017) stressed the importance of the temperature of the underlying surface in controlling the boundary-layer convection. In wintertime storms in the North-East Atlantic region, such convection is most likely to occur where an airstream crosses an increasingly warm sea. However, surface heat fluxes are not always sufficient to generate convection, especially inland in winter and overnight. This is why a mechanism for cooling the air in the LLJ just above the boundary layer can be so important. We have shown in the present study that the cooling occurred in the airstream forming the LLJ over a period of about 5 hours as a result of slow descent and the evaporation of the upper part of a nearby layer of mixed-phase cold-frontal cloud– in fact the very same frontal cloud that later developed into a cloud head. The total cooling amounted to as much as 4 to 5 C over the 5-hour period because the source of cloud for evaporation was continually being renewed. The mechanism for bringing the cloud particles into this region is unresolved.

The main effect of the evaporation was to increase substantially the convective instability where the resulting cooled airstream eventually overran the shallow moist zone (SMZ) in the warm sector. This evaporative cooling also led to the generation of a significant (positive) potential vorticity (PV) anomaly owing to an increase in the static stability just above where the evaporative cooling initially took place. These twin layers of cloud-top cooling and PV generation form what we have termed the *diabatically modified cloud top layer*, DMCTL.

There have been previous studies of the effects of diabatic heating rates (DHRs) on the generation of PV in situations of slantwise frontal ascent (*e.g.* Joos and Wernli 2012; Joos and Forbes 2016), but these have emphasized the diabatic cooling beneath the region of slantwise ascent rather than that above the layer of slantwise ascent as in the present case. The occurrence of a layer of evaporative cooling at the top of the slantwise ascent is probably less common than the well known layer of evaporative cooling that often occurs beneath the slantwise ascent but, when it does occur, we have shown that it can have important effects. In the present study, the location of the evaporative heat sink above the main condensation heat source in the slantwise ascent led to a characteristic signature in the distribution of PV within the frontal cloud layer. This was in the form of a split PV distribution in which the upper limb of the positive PV anomaly is attributable to the effect of evaporation in the upper part of the cloud layer. The PV anomaly was advected to a position near the upper part of the convective rainbands at a height of 2 km, at which time it was 0.5 to 1.0 km deep and 100 to 150 km wide.

Browning *et al.* (1997), in their study of an extratropical cyclone undergoing frontal fracture, found that the field of θ_w at low levels was distorted by rotation (about a vertical

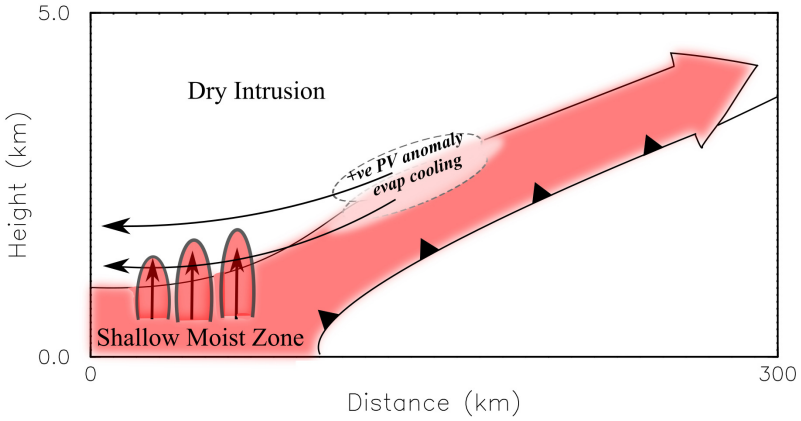

Figure 13. Conceptual model of a cloud-top cooling mechanism for triggering convection in the shallow moist zone (SMZ) of the warm sector of an extratropical cyclone, showing the component of flow within a vertical section orientated south-north in a cyclone travelling west-to-east. The two dashed ellipses labelled '+ve PV anomaly' and 'evap cooling' at the top of the ana-cold frontal ascent (shaded arrow) together constitute the diabatically modified cloud-top layer (DMCTL). This air descends along the thin arrows to a position above the SMZ, triggering shallow but vigorous convection there. (There are also other layers of diabatic PV within and below the shaded ascent owing to condensation within the ascending flow and evaporation beneath it– see Figure 11 of Chagnon *et al.* (2013). These are not part of the mechanism discussed here and are not shown in the present figure.)This figure to be available in colour in the online article.

axis) which increased with height. This differential rotation led to increasingly forward-tilted θ_w surfaces, and hence increased the potential instability, where the DI overran the SMZ in the warm sector. They suggested that the differential rotation with height was induced by a local maximum of potential vorticity aloft within a tropopause fold. Griffiths *et al.* (2000) followed this up using the technique of PV-inversion and demonstrated that convective destabilization by differential wrapping-up of θ_w surfaces could indeed be produced by an overlying tropopause fold. Our present study was carried out for a storm which had not yet entered the stage of frontal fracture and there was no pronounced fold. There was a tropopause depression which may have had some effect in destabilizing the lower levels, but we suspect that the potential vorticity anomaly that originated in the DMCTL would have been more influential in enhancing convective destabilization because it ended up being so close to the observed boundary-layer convection. In their study of a convective precipitation band, Novak *et al.* (2009) found that differential advection in a dry slot was not responsible for the relevant destabilization, but in the present study the PV anomaly was probably much closer to the level of convection.

5. Conclusions

The principal results of this case study are summarized in the conceptual model in Figure 13. The broad shaded arrow in Figure 13 shows air with high wet-bulb potential temperature from the shallow moist zone (SMZ) of a warm sector rising into the very dry air of a dry intrusion (DI). This air rises slantwise above a cold frontal zone and forms an ana-cold frontal cloud band and an associated wide cold-frontal rainband. Chagnon *et al.* (2013)- see their Figure 11) showed that condensation within this ascent and evaporation in the underlying dry air leads to a dipole of heating/cooling, which creates a tripole of PV across the frontal zone. The dynamical impacts of this are well known (*e.g.* Joos and Wernli, 2012) but it is not the focus of the present study and is not represented in Figure 13. Instead, the focus here has been on a smaller region at the top of the ascending layer. Sometimes, as in the present case study, a localized region of descent develops, leading to an area of sustained evaporative cooling within an upper part of the cloud layer (small dashed area in Figure 13 labelled 'evap. cooling'). This evaporation also generates a positive anomaly of PV just above it (small dashed area labelled '+ve PV anomaly'). We refer to the air originating within these small dashed regions as the diabatically modified cloud-top layer (DMCTL).

We have shown in this case study that the air from the DMCTL descended slantwise at the top of the cloud deck and continued to undergo evaporative cooling so that, by the time it overran the SMZ, its dry-bulb potential temperature had diminished by up to almost 5 C. This increased the convective instability and led to shallow but vigorous boundary-layer convection.

Air starting in the small dashed region labelled '+ve PV anomaly' in Figure 13 descended slantwise just above the evaporatively cooled air and, again over a period of about 5 hours, its PV increased to as much as 3 PVU. It is possible that this PV anomaly, as a result of its eventual proximity to the boundary layer was associated with differential flows below it which further increased the convective instability and hence the vigour of the boundary-layer convection. The evaporatively enhanced convection is important in situations when there are strong winds just above the boundary layer because it can help transport high momentum downwards, leading to damaging surface winds. In the present case the strong winds were due mainly to the overall westerly component of the wind, *i.e.* the component normal to the plane of the diagram.

Whilst this paper unequivocally identifies a role for evaporative cooling in invigorating the warm-sector convection, we have not quantified how important the generation of the PV anomaly by the evaporative cooling actually was in further destabilizing the boundary-layer convection; an investigation using PV inversion techniques would be required to resolve this issue.

The present study related to an early stage of an extratropical cyclone before it had developed significantly. In other research (Browning *et al.* 2015) a similar role for evaporative cooling in destabilizing the boundary layer was identified in a rapidly deepening cyclone at the stage of frontal fracture. Destabilization of the boundary layer can be due to the evaporative cooling mechanism as in these studies or to surface fluxes if the underlying surface is warm enough (Slater *et al.* 2017). Further research is required to establish the relative importance of these mechanisms but, one way or another, a destabilized boundary layer is an important ingredient of situations when extratropical storms produce damaging surface winds.

Acknowledgements

We are grateful to Professors David Schultz and Alan Thorpe for helpful comments on an earlier draft and to two anonymous referees for detailed criticisms. ERA–Interim data were provided courtesy of ECMWF.

References

Böttger H, Eckardt M, Katergiannakis U. 1975. Forecasting extra-tropical storms with hurricane intensity using satellite information. *J.Appl. Meteorol.,* **14**: 1259–1265.

Browning KA. 1995. On the nature of the mesoscale circulation at a kata-cold front. *Tellus,* **47A**: 911–919.

Browning KA. 1997. The dry intrusion perspective of extratropical cyclone development. *Meteorol. Appl.,* **4**: 317–324.

Browning KA. 2004. The sting at the end of the tail: Damaging winds associated with extratropical cyclones. *Q. J. R. Meteorol. Soc.,* **130**: 375–399. doi: 10.1256/qj.02.143.

Browning KA, Ballard SP, Davitt CSA. 1997. High-resolution analysis of frontal fracture. *Mon.Wea.Rev.,* **125**: 1212–1230.

Browning KA, Monk GA. 1982. A simple model for the synoptic analysis of cold fronts. *Q.J.R. Meteorol. Soc.,* **108**: 435–452.

Browning KA, Roberts NM. 1999. Mesoscale analysis of arc rainbands in a dry slot. *Q.J.R. Meteorol. Soc.,* **125**: 3495–3511.

Browning KA, Smart DJ, Clark MR, Illingworth AJ. 2015. The role of evaporating showers in the transfer of sting-jet momentum to the surface. *Q. J. R. Meteorol. Soc.,* **141**: 2956–2971.

Carr FH, Millard JP. 1985. A composite study of comma clouds and their association with severe weather over the Great Plains. *Mon.Wea.Rev.,* **113**: 370–387.

Chagnon J M, Gray SL, Methven J. 2013. Diabatic processes modifying potential vorticity in a North Atlantic cyclone. *Q. J. R. Meteorol. Soc.,* **139**: 1270–1282.

Clark PA, Browning KA, Wang CG. 2005. The sting at the end of the tail: Model diagnostics of fine-scale three-dimensional structure of the cloud head. *Q. J. R. Meteorol. Soc.,* **131**: 2263–2292.

Clough SA, Franks RAA. 1991. The evaporation of frontal and other stratiform precipitation. *Q. J. R. Meteorol. Soc.,* **117**: 1057–1080.

Coronel B, Ricard D, Riviere G, Arbogast P. 2016. Cold-conveyor-belt jet, sting jet and slantwise circulations in idealized simulations of extratropical cyclones. *Q. J. R. Meteorol. Soc.,* **142**: 1781–1796.

Dee D P, Co-authors. 2011. The ERA-Interim reanalysis: configuration and performance of the data assimilation system. *Q.J.R. Meteorol. Soc.,* **137**: 553–597. doi:10.1002/qj.828.

Gray SL, Martínez-Alvarado O, Baker LH, Clark PA. 2011. Conditional symmetric instability in sting-jet storms. *Q. J. R. Meteorol. Soc.,* **137**: 1482–1500.

Griffiths M, Thorpe AJ, Browning KA. 2000. Convective destabilisation by a tropopause fold diagnosed using potential vorticity inversion. *Q. J. R. Meteorol. Soc.,* **126**: 125–144.

Hewson TD, Neu U. 2015. Cyclones, windstorms and the IMILAST project. *Tellus,* **67A**: 27–42.

Joly A, Co-authors. 1999. Overview of the field phase of the Fronts and Atlantic Storm-Track EXperiment (FASTEX) project. *Q.J.R. Meteorol. Soc.,* **125**: 3131–3163.

Joos H, Forbes RM. 2016. Impact of different IFS microphysics on a warm conveyor belt and the downstream flow evolution. *Q.J.R. Meteorol. Soc.,* **142**: 2727–2739.

Joos H, Wernli H. 2012. Influence of microphysical processes on the potential vorticity development in a warm conveyor belt: A case-study with the limited-area model COSMO. *Q.J.R. Meteorol. Soc.,* **138**: 407–418.

Novak DR, Colle BA, McTaggart-Cowan R. 2009. The role of moist processes in the formation and evolution of mesoscale snowbands within the comma head of Northeast U.S. cyclones. *Mon.Wea.Rev.,* **137**: 2662–2686.

Shapiro MA, Keyser D. 1990. Fronts, Jet Streams and the Tropopause. *Extratropical Cyclones: The Erik Palmén Memorial Volume.* Ed. C W Newton and E O Holopainen. American Meteorological Society: Boston, MA; pp 167–191.

Skamarock WC, Klemp JB, Dudhia J, Gill DO, Barker DM, Duda MG, Huang X-Y, Wang W and Powers JG. 2008. A Description of the Advanced Research WRF Version 3. *NCAR Technical Note*, NCAR/TN-475+STR.

Slater TP, Schultz DM, Vaughan, G. 2015. Acceleration of near-surface strong winds in a dry, idealised cyclone. *Q.J.R. Meteorol. Soc.,* **141**: 1004–1016.

Slater TP, Schultz DM, Vaughan, G. 2017. Near-surface strong winds in a maritime extratropical cyclone: acceleration of the winds and the importance of surface fluxes. *Q.J.R. Meteorol. Soc.,* **143**: 321–332. doi:10.1002/qj.2924.

Smart DJ, Browning KA. 2014. Attribution of strong winds to a cold conveyor belt and sting jet. *Q.J.R. Meteorol. Soc.,* **140**: 595–610. doi: 10.1002/qj.2162.

Stoelinga MT. 2009. A users guide to RIP version 4. *Technical Note*. University of Washington: Seattle, WA.

Thorpe AJ, Clough SA. 1991. Mesoscale dynamics of cold fronts: Structures described by dropsoundings in FRONTS 87. *Q. J. R. Meteorol. Soc.,* **117**: 903–941.

Vaughan G, Co-authors.2015. Cloud Banding and Winds in Intense European Cyclones: Results from the DIAMET Project. *Bull. Amer. Met. Soc.,* **96**: 249–265.

Young MV, Monk GA, Browning KA. 1987. Interpretation of satellite imagery of a rapidly deepening cyclone. *Q.J.R. Meteorol. Soc.,* **113**: 1089–1115.